Mesoscopic Structure Prediction of Nanoparticle Assembly and Co-Assembly : Theoretical foundation

Kahyun Hur,[1] Richard G. Hennig,[1] Fernando A. Escobedo,[2] and Ulrich Wiesner[1]

[1]Department of Material Science and Engineering, Cornell University, Ithaca, NY, 14853

[2]School of Chemical and Biomolecular Engineering, Cornell University, Ithaca, NY, 14853

Abstract

In this work, we present a theoretical framework that unifies polymer field theory and density functional theory in order to efficiently predict ordered nanostructure formation of systems having considerable complexity in terms of molecular structures and interactions. We validate our approach by comparing its predictions with previous simulation results for model systems. We illustrate the flexibility of our approach by applying it to hybrid systems composed of block copolymers and ligand coated nanoparticles. We expect that our approach will enable the treatment of multi-component self-assembly with a level of molecular complexity that approaches experimental systems.

PACS: 81.16.Dn,81.16.Fg

Manuscript text

1. Introduction

Nanoparticle (NP) assembly and co-assembly are topics of significant current scientific interest due to their potential impact on the engineering of new materials. Recent advances in synthesis allow the growth of monodisperse NPs from a wide range of solids, *e.g.* metals, semiconductors, and insulators.[1-5] This control enables ordered crystal formation, including binary superlattices at the mesoscopic scale (1 to 1000 *nm*), thus providing powerful modular pathways to the design of 'metamaterials' that should ultimately result in devices with programmable chemical and physical properties.[6-9] NP formation and assembly has also been found to play a critical role in natural biomineralization processes. It recently has been shown that amourphous calcium carbonate (ACC) NPs nucleate in solution and assemble at an ordered template of macromolecules thus challenging classical crystallization theories.[10-11] Similar NP assembly behavior is currently utilized in the field of synthetic porous solids.[12] Aside from oxide structures mesoporous bulk metals are formed from block copolymer (BCP) / metal NP self-assembly through careful tailoring of particle-polymer-solvent and particle-particle interactions.[13] In many of these experimental systems, chemical building blocks are complex organic/inorganic hybrid molecules such as ligand-stabilized NPs. Furthermore, Coulomb or dipolar long-range particle-particle interactions are believed to play an essential role in their assembly. In particular for complex multi-component systems involving assembly of NPs and macromolecules, limited understanding of the role of such key factors has severely hampered progress. Clearly, better predictive theoretical and simulation methods are needed.

To this end, we present an efficient theoretical framework that unifies polymer field theory and density functional theory (DFT) into a single method in order to incorporate complex

molecular details with key physical interactions. Atomistic or particle-based modeling such as molecular dynamics and Monte Carlo (MC) simulations can readily incorporate different molecular details but are computationally more expensive than field-theoretical approaches. Furthermore, they require specialized methods to measure or impose chemical potentials and an analysis of finite system-size effects to ensure that structures at thermodynamic equilibrium are obtained (*e.g.*, some morphological features can be frustrated by a lack of geometric commensurability with the box dimensions).[14-18] Alternatively, the morphologies of BCP self-assembly have been successfully studied and predicted by self-consistent field theory (SCFT),[14,19-23] a field theoretic description of chemical fields exploiting the mean-field approximation.[21] Shi *et al.*[56] and Wang *et al.*[57] proposed SCFT approaches to simulate polyelectrolyte by incorporating Coulomb interactions between polymer segments. The SCFT approach is very efficient and powerful, but the original SCFT approach is not readily applicable to systems beyond BCP self-assemblies due to its inability to describe the interactions associated with NPs. A combined approach of atomistic and field theoretic modeling as well as a novel MC approach have been suggested for simulation of BCP/NP self-assembly,[24] but they have the same or similar limitations found in atomistic simulations. Meanwhile, DFT approaches were suggested for different molecular systems,[25-27] but their applications were limited to local structure prediction. Thompson *et al.* introduced a new numerical scheme of combining SCFT with DFT.[28-29] The SCFT/DFT approach seems quite promising for investigating the equilibrium properties of BCP/NP composites, but its application has been limited to simple mixture systems of BCPs and hard sphere (HS) particles.[28-30] Due to the difficulties in describing arbitrary types of molecular structures and interactions, applications of field theoretic approaches to more complex molecular systems such as those systems with charged NPs or ligand-stabilized NPs

remain a significant challenge.

In order to overcome such limitations of existing theories, we extend the Green function propagator to hard particles and incorporate key physical interactions in the form of direct correlation functions for complex molecular systems. The Green function propagator approach has been used to describe polymer configurations in polymer field theory, but their applications have been limited to polymers. By using this propagator we introduce a theoretical framework that enables us to integrate not only discrete but also continuous segments into a molecule. The framework offers greater flexibility to incorporate complex molecules composed of soft and hard chemical species than existing SCFT, SCFT/DFT, and other polymer DFT approaches.[27,46] The direct correlation functions are widely used in well-established DFT approaches.[31] Atomistic interactions such as Coulomb,[32-34] Yukawa,[33] dipole,[34] and Lennard-Jones interactions[33,35] can be incorporated in this context. Therefore, our approach enables us to incorporate the complexity of molecular structures and their interactions while taking advantage of the efficiency of field theories for sampling phase space of molecular systems. We demonstrate the validity of our approach by first comparing its predictions with previous results[28] and then applying it to a hybrid materials system consisting of multi-component molecules with NPs. Further applications of our approach will be presented elsewhere.[36]

2. Theoretical and numerical procedures

2.1. Overview

Our field-theoretic approach is based on the minimization of the Helmholtz free energy functional, $F[\rho, w]$, of a system with respect to variations of the density functions, ρ, and chemical fields, w. The general schematic procedure and key equations are summarized in Fig.

1. In Sections 2.2 and 2.3, F is obtained from the particle-based partition function, where interactions are added to the excess free energy functional, F^{ex}, in a functional form. Various interactions can be incorporated following Eq. (11). The process is similar to that of incorporating different force field terms in particle-based simulations. The most general form of F for the present work is given as Eqs. (9) and (13). In Sections 2.3 and 2.4, the chemical fields, w, given in Eqs. (14) and (18) are obtained from the functional derivative of F with respect to ρ. In Section 2.5, the density functions, ρ, are obtained from the functional derivative of F with respect to w, see Eq. (40). It is shown that ρ can be calculated from the single molecular partition function Q and the segment distribution functions, q and $q^\dagger$. To obtain Q, q and $q^\dagger$, we introduce the Green's function, G, that propagates from one segment to another as i to $i+1$ in Fig. 2. The density distribution functions q and $q^\dagger$ for each segment are calculated from their convolution with G via Eqs. (34) and (35) with the boundary conditions given by Eqs. (37) and (38). In Section 2.6, q, $q^\dagger$, and G are formulated for continuous segments, see Eqs. (44), (47), and (48). For each step in the calculations outlined in Fig. 1, w and ρ are updated iteratively until changes of $\rho(\mathbf{r})$ and $w(\mathbf{r})$ become sufficiently small. Finally, in Section 2.7, field theories beyond the mean-field approximation in Section 2.7 are considered.

2.2. Helmholtz free energy functional

For clarity, we only present the equations derived for a homogeneous system with one type of molecule; the extension to inhomogeneous mixture systems is straightforward. The configurational partition function of the canonical ensemble is given by

$$Z = \frac{1}{n!}\int d\mathbf{r}^n P\left(\mathbf{r}^n\right) E\left(\mathbf{r}^n\right) R\left(\mathbf{r}^n\right) \exp\left[-U\left(\mathbf{r}^n\right)/k_B T\right], \tag{1}$$

where n is the number of molecules, $R\left(\mathbf{r}^n\right)$ is the incompressibility constraint term, $U\left(\mathbf{r}^n\right)$ is the interaction potential, and $k_B T$ is the Boltzmann constant multiplied by the temperature (note that we neglect unimportant constant terms such as the de Broglie thermal wavelength). The term $P\left(\mathbf{r}^n\right)$ accounts for the molecular configuration of multi-component molecules such as polymers or hybrid molecules (see discussion in Section 2.5). For hard particle interactions, the excluded volume constraint, $E\left(\mathbf{r}^n\right)$, is included. For multi-component molecules, we specify each monomer species with a parameter, i. The density operator of the ith monomer species, $\hat{\rho}_i\left(\mathbf{r}\right)$, for multi-component molecules is given by

$$\hat{\rho}_i\left(\mathbf{r}\right) = \sum_j^n \delta\left[\mathbf{r} - \mathbf{r}_i^j\right], \tag{2}$$

where $\mathbf{r}_i^j$ is the positional vector of the monomer species i of molecule j. Consequently, $U\left(\mathbf{r}^n\right)$ is given by

$$U\left(\mathbf{r}^n\right) = \frac{1}{2}\sum_{i,j}\iint d\mathbf{r} d\mathbf{r}' \hat{\rho}_i\left(\mathbf{r}\right) u_{ij}\left(\mathbf{r},\mathbf{r}'\right) \hat{\rho}_j\left(\mathbf{r}'\right), \tag{3}$$

where $u_{ij}\left(\mathbf{r},\mathbf{r}'\right)$ is a pair potential function describing the interaction between monomer species i at $\mathbf{r}$ and j at $\mathbf{r}'$. For example, $u_{ij}\left(\mathbf{r},\mathbf{r}'\right)$ for Coulomb interactions between point charges is

given by $u_{ij}(\mathbf{r},\mathbf{r}') = Z_i Z_j / 4\pi\varepsilon|\mathbf{r}-\mathbf{r}'|$, where Z_i and Z_j are charges of species i and j respectively, and ε is the permittivity. The 2nd order direct correlation function defined by $C_{ij}(\mathbf{r},\mathbf{r}') = -1/k_B T \cdot D^2 F^{ex} / D\rho_i(\mathbf{r}) D\rho_j(\mathbf{r}')$ in Sections 2.3 and 2.4 has a meaning consistent with $-u_{ij}(\mathbf{r},\mathbf{r}')/k_B T$, where $F^{ex}[\rho]$ is the 'excess' free energy functional and the free energy contributions of pair-wise interactions between particles (noting that $DF/D\rho$ denotes the functional derivative of the functional $F[\rho]$). Higher order direct correlation functions than 2nd order can be neglected for slowly varying potentials such as the Coulomb potential without significant loss of accuracy,[33] since they are related to multi-body interactions. The excluded volume constraint $E(\mathbf{r}^n)$ in Eq. (1) is also included in the excess free energy functional form as in Section 2.4. Therefore, particle-particle interactions including enthalpic interactions and purely entropic excluded volume interactions are given in the form of the excess free energy functional. In field theoretic approaches, the partition function Z is re-expressed in terms of local densities, $\rho(\mathbf{r})$, and chemical potential fields, $w(\mathbf{r})$, using the identities for the delta functional,[20,37]

$$\int D\rho_i \delta[\rho_i - \hat{\rho}_i] = 1 \tag{4}$$

and

$$\delta[\rho_i - \hat{\rho}_i] = \int Dw_i \exp\left[\int d\mathbf{r} w_i(\mathbf{r})\{\rho_i(\mathbf{r}) - \hat{\rho}_i(\mathbf{r})\}\right], \tag{5}$$

where D represents the functional integral. Then Z for the field theoretic description takes the form

$$Z = \frac{C}{n!}\int D\xi \left(\prod_i^N D\rho_i Dw_i \exp\left\{ \int d\mathbf{r} w_i(\mathbf{r})\rho_i(\mathbf{r}) \right\} \right) \\ \times Q^n\left[\{w\}\right] \exp\left\{ \int d\mathbf{r}\xi(\mathbf{r}) \left[1 - \sum_i^N \varphi_i(\mathbf{r}) \right] \right\} \exp\left[-\frac{1}{k_B T} F^{ex} \right] \tag{6}$$

where C is the normalization constant, N is the number of monomer species in one molecule, and Q is the single molecular partition function discussed in Section 2.5. The excess free energy functional F^{ex} details interactions between particles as $U(\mathbf{r}^n)$ in Eq. (1) and will be discussed more detail in Section 2.3. The incompressibility term, $R(\mathbf{r}^n)$, in Eq. (1) is given in a functional form,

$$\delta\left(1 - \sum_i^N \varphi_i(\mathbf{r})\right) = \int D\xi \exp\left\{ \int d\mathbf{r}\xi(\mathbf{r}) \left[1 - \sum_i^N \varphi_i(\mathbf{r}) \right] \right\}, \tag{7}$$

satisfying the incompressibility condition,

$$\sum_i^N \varphi_i(\mathbf{r}) = 1, \tag{8}$$

where $\varphi_i(\mathbf{r})$ is the local volume fractional functional of the i th monomer species, obtained from its density function, $\rho_i(\mathbf{r})$, by convolution with its shape function, $S_i(\mathbf{r})$, defined as $S_i(\mathbf{r}) = \rho_0^{-1}\delta(|\mathbf{r}|)$ for point-like monomer species, and $S_i(\mathbf{r}) = H(R_i - |\mathbf{r}|)$ for spherical monomer species, where ρ_0^{-1} is the reference volume for point-like monomer species, $\delta(x)$ is

the Dirac delta function, $H(x)$ is the Heaviside step function, and R_i is the radius of the spherical monomer species i. The $\xi(\mathbf{r})$ is a Lagrange multiplier function that needs to be chosen to satisfy Eq. (8). The Helmholtz free energy functional, F, is given as

$$F[\rho, w] = F^0[\rho, w] + F^{ex}[\rho], \tag{9}$$

where F^0 describes the mixing and conformational entropy as well as the pressure energy, and is obtained from

$$\begin{aligned} F^0 / k_B T = & -n \ln Q[\{w\}] - \sum_i \left\{ \int d\mathbf{r} w_i(\mathbf{r}) \rho_i(\mathbf{r}) \right\} \\ & - \int d\mathbf{r} \xi(\mathbf{r}) \left[1 - \sum_i \varphi_i(\mathbf{r}) \right] \end{aligned}, \tag{10}$$

where we neglect unimportant constant terms for clarity. When the incompressibility condition is satisfied, the last term of Eq. (10) vanishes.

2.3. The excess free energy functional

F^{ex} in Eq. (9) primarily contains the enthalpic interactions between all species but also includes purely entropic hard sphere (HS) interaction terms (hence the notation of 'excess' instead of 'enthalpic'); in its most general form it is given by:

$$F^{ex} = F^{\chi} + F^{HS} + F^{C} + F^{Dipole} + F^{Yukawa} + \cdots. \tag{11}$$

The conventional SCFT approach[14,19-23,38-39] only includes the first term describing short range enthalpic interactions, F^{χ}. A combined SCFT/DFT approach was recently developed to also implement short range HS interactions, F^{HS}, in addition to F^{χ}.[28-30] In order to describe more realistic experimental systems, long range interactions such as Coulomb, F^{C}, dipole, F^{Dipole}, and screened Coulomb interactions, F^{Yukawa}, have to be included. By choosing Coulomb interactions as an example, here we introduce our strategy to implement such long range interactions. The excess free energy functional is obtained as

$$\begin{aligned} F^{ex}/k_BT = &\sum_{i<j}\rho_0\chi_{ij}\iint d\mathbf{r}d\mathbf{r}'\varphi_i(\mathbf{r})\varphi_j(\mathbf{r}')+\int d\mathbf{r}\Phi^{HS}\left[\{\rho\};\mathbf{r}\right] \\ &-\frac{1}{2}\sum_{ij}\iint d\mathbf{r}d\mathbf{r}'\rho_i(\mathbf{r})C_{ij}^{C}(\mathbf{r},\mathbf{r}')\rho_j(\mathbf{r}') \end{aligned}, \tag{12}$$

where the first term represents F^{χ}, the second term F^{HS}, and the last term F^{C}. Here C_{ij}^{C} is the direct correlation function for Coulomb interactions.[33] By combining Eqs. (10) and (12), the Helmholtz free energy functional, F, is obtained as

$$\begin{aligned} F/k_BT = &-n\ln Q\left[\{w\}\right]-\sum_i\left\{\int d\mathbf{r}w_i(\mathbf{r})\rho_i(\mathbf{r})\right\} \\ &-\int d\mathbf{r}\xi(\mathbf{r})\left[1-\sum_i\varphi_i(\mathbf{r})\right] \\ &+\sum_{i<j}\rho_0\chi_{ij}\iint d\mathbf{r}d\mathbf{r}'\varphi_i(\mathbf{r})\varphi_j(\mathbf{r}')+\int d\mathbf{r}\Phi^{HS}\left[\{\rho\};\mathbf{r}\right] \\ &-\frac{1}{2}\sum_{ij}\iint d\mathbf{r}d\mathbf{r}'\rho_i(\mathbf{r})C_{ij}^{C}(\mathbf{r},\mathbf{r}')\rho_j(\mathbf{r}') \end{aligned}, \tag{13}$$

where the first three terms in the right hand side represent the entropic part, F^{0}, and the last three terms represent the excess part, F^{ex}, for short-range enthalpic, HS, and long-range

Coulomb interactions, respectively. The Helmholtz free energy functional, F, is not directly used in the self-consistent iteration process, but is evaluated for obtaining the system with the lowest free energy as shown in Fig. 1. Applying the mean-field approximation,[21,38] the average chemical potential field felt by the ith monomer, $w_i(\mathbf{r})$, is obtained at saddle points of F, where $DF / D\rho_i(\mathbf{r}) = 0$, and is given by

$$w_i(\mathbf{r}) = \left[\mu_i^{\chi}(\mathbf{r}) + \mu_i^{HS}(\mathbf{r}) + \mu_i^{C}(\mathbf{r})\right] / k_B T + \Xi_i(\mathbf{r}). \tag{14}$$

where $\mu_i^{\chi}(\mathbf{r})$, $\mu_i^{HS}(\mathbf{r})$, and $\mu_i^{C}(\mathbf{r})$, are the chemical potential fields of short range enthalpic, short range HS, and long range Coulomb interactions, respectively, and $\Xi_i(\mathbf{r})$ is the pressure field for monomer i. As in the conventional SCFT, short range enthalpic interactions between distinct chemical species are described by dimensionless Flory-Huggins interaction parameters, χ_{ij}, and the first term in Eq. (14), $\mu_i^{\chi}(\mathbf{r})$, is given by

$$\mu_i^{\chi}(\mathbf{r}) / k_B T = \frac{\rho_0}{N} \int d\mathbf{r}' S_i(\mathbf{r}' - \mathbf{r}) \sum_{i \neq j} \chi_{ij} N \varphi_j(\mathbf{r}'). \tag{15}$$

Here we use χ_{ij} parameters for the short range enthalpic interactions, since experimental solubility parameters can be directly applied as simulation parameters. We utilize the fundamental measure theory (FMT) approach[39] for short range HS interactions described by the second term, $\mu_i^{HS}(\mathbf{r})$ in Eq. (14), as outlined in Ref. 33 and repeated in Section 2.4. The third term in Eq. (14), $\mu_i^{C}(\mathbf{r})$, describes the long-range Coulomb interactions and is obtained from the

direct correlation function as

$$\mu_i^C(\mathbf{r})/k_BT = -\sum_j \int d\mathbf{r}' C_{ij}^C(\mathbf{r},\mathbf{r}')\rho_j(\mathbf{r}'), \tag{16}$$

The non-negligible contribution of the long range Coulomb potential tail on the chemical field is efficiently computed via the Ewald summation technique.[31] Thus, long range interactions can be incorporated into the theory by using direct correlation functions and the Ewald summation technique, which is discussed in Section 2.4. Other long-range interactions such as screened Coulomb,[33] dipole,[34] and Lennard-Jones interactions[33,35] can be included in the theory in the same way as the Coulomb interaction case exemplified here. Finally, the last term in Eq. (14), $\Xi_i(\mathbf{r})$, is given by

$$\Xi_i(\mathbf{r}) = \frac{\rho_0}{N}\int d\mathbf{r}'\xi(\mathbf{r}')S_i(\mathbf{r}'-\mathbf{r}). \tag{17}$$

Combining Eqs. (15), (16), and (17) yields the chemical fields felt by monomer species i

$$\begin{aligned} w_i(\mathbf{r}) = {} & \frac{\rho_0}{N}\int d\mathbf{r}'\left[\sum_j \chi_{ij}N\varphi_j(\mathbf{r}')+\xi(\mathbf{r}')\right]S_i(\mathbf{r}'-\mathbf{r}) \\ & +\mu_i^{HS}(\mathbf{r})/k_BT - \sum_j \int d\mathbf{r}' C_{ij}^C(\mathbf{r},\mathbf{r}')\rho_j(\mathbf{r}') \end{aligned}. \tag{18}$$

2.4. Density Functional Form

To account for excluded volume interactions in our field theoretic approach, we include

the excluded volume constraint, $E\left(\mathbf{r}^n\right)$, in Eq. (1) that particles cannot concurrently occupy the same space. In contrast to other interactions, hard-particle interactions are purely entropic. Unfortunately, there is no exact analytic solution for 3-dimensional systems. Instead, Percus obtained an exact result for the free energy density of 1-dimensional hard rods.[40] Although the 1-dimensional result is not widely useful in itself, it is an important starting point for evaluating other hard-particle interactions.[41] The FMT method pioneered by Rosenfeld for hard-particle interactions in 3 dimensions is based on Percus' result.[39] In the present work, we utilize the FMT since it is the most advanced hard particle DFT for inhomogeneous hard body systems.[41] The FMT was originally developed for inhomogeneous mixture systems of HSs. It supersedes other approaches in (i) providing flexibility for incorporating inhomogeneous hard particle mixtures, and in (ii) providing accurate predictions for dense packing behaviors, *e.g.* liquid to solid transitions, of hard particles.[41-42] The excess free energy functional is given as $F^{HS}/k_BT=\int d\mathbf{r}\Phi^{HS}\left(\mathbf{r}\right)$, where the excess free energy density, Φ^{HS}, is obtained from

$$\begin{aligned}\Phi^{HS}\left(\mathbf{r}\right)&=-n_0\ln\left(1-n_3\right)+n_1n_2/\left(1-n_3\right)+n_2^3/\left(1-n_3\right)^2/\left(24\pi\right)\\&-\mathbf{n}_{V1}\cdot\mathbf{n}_{V2}/\left(1-n_3\right)-n_2\left(\mathbf{n}_{V1}\cdot\mathbf{n}_{V2}\right)/\left(1-n_3\right)^2/\left(8\pi\right)\end{aligned}. \tag{19}$$

Φ^{HS} is a function of the weighted densities, n_α, which are given by

$$n_\alpha\left(\mathbf{r}\right)=\sum_i\int d\mathbf{r}'\rho_i\left(\mathbf{r}'\right)W_i^{(\alpha)}\left(\mathbf{r}-\mathbf{r}'\right), \tag{20}$$

where the weighting functions are $W_i^{(3)}\left(\mathbf{r}\right)=H\left(R_i-\left|\mathbf{r}\right|\right)$, $W_i^{(2)}\left(\mathbf{r}\right)=\delta\left(R_i-\left|\mathbf{r}\right|\right)$,

$\mathbf{W}_i^{(V2)}(\mathbf{r}) = \frac{\mathbf{r}}{|\mathbf{r}|}\delta(R_i - |\mathbf{r}|)$, $W_i^{(1)}(\mathbf{r}) = W_i^{(2)}(\mathbf{r})/4\pi R_i$, $W_i^{(0)}(\mathbf{r}) = W_i^{(2)}(\mathbf{r})/4\pi R_i^2$, and $\mathbf{W}_i^{(V1)}(\mathbf{r}) = \mathbf{W}_i^{(V2)}(\mathbf{r})/4\pi R_i$ and R_i is the radius of HS particle i. The excess chemical potential functional is obtained as

$$\mu_i^{HS}(\mathbf{r})/k_BT = \int d\mathbf{r}' \sum_\alpha \mu_\alpha W_i^{(\alpha)}(\mathbf{r}' - \mathbf{r}), \tag{21}$$

where $\mu_\alpha = \partial\Phi^{HS}/\partial n_\alpha$ and

$$\begin{aligned}
&\mu_0 = -\ln(1-n_3),\\
&\mu_1 = n_2/\ln(1-n_3),\\
&\mu_2 = n_1/(1-n_3) + (1/8\pi)n_2^2/(1-n_3)^2\\
&-(1/8\pi)\mathbf{n}_{V2}\cdot\mathbf{n}_{V2}/(1-n_3)^2,\\
&\mu_3 = n_0/(1-n_3) + n_1n_2/(1-n_3)^2\\
&-(1/12\pi)n_2^3/(1-n_3)^3 - \mathbf{n}_{V1}\cdot\mathbf{n}_{V2}/(1-n_3)^2\\
&-(1/4\pi)n_2\mathbf{n}_{V2}\cdot\mathbf{n}_{V2}/(1-n_3)^3,\\
&\mu_{V1} = -\mathbf{n}_{V2}/(1-n_3),\\
&\mu_{V2} = -\mathbf{n}_{V1}/(1-n_3) - (1/4\pi)n_2\mathbf{n}_{V2}/(1-n_3)^2
\end{aligned} \tag{22}$$

The direct correlation function for the Coulomb potential, $V(\mathbf{r})/k_BT = \Gamma Z_iZ_j/|\mathbf{r}|$, was obtained based on the mean-spherical approximation.[42] The direct correlation function, C_{ij}^C, for charged HS particles can be interpreted as the effective interaction between two spherical cavities with the radii, R_i and R_j, where charges are uniformly distributed.[33] Blum's theory for C_{ij}^C is also

based on interactions between two spherical charged cavities with radii increased as much as the capacitance length.[32,43-44] In this work, we use Rosenfeld's formulation of the direct correlation function[42] which is given by

$$C_{ij}^{C}\left(\mathbf{r}_i,\mathbf{r}_j\right)=-Z_iZ_j\Gamma\iint d\mathbf{r}'d\mathbf{r}''W_i^{(2)}\left(\mathbf{r}_i-\mathbf{r}'\right)W_j^{(2)}\left(\mathbf{r}_j-\mathbf{r}''\right)/\left|\mathbf{r}'-\mathbf{r}''\right| \tag{23}$$

and

$$\frac{-C_{ij}^{C}\left(\mathbf{r},\mathbf{r}'\right)}{Z_iZ_j\Gamma}=\begin{cases}2B_0\left(R_i+R_j-\tau_{ij}\right), \text{ if } \left|\mathbf{r}-\mathbf{r}'\right|<\tau_{ij}\\ 2B_0\left(R_i+R_j-\tau_{ij}\right)-B_0\left(\left|\mathbf{r}-\mathbf{r}'\right|-\tau_{ij}\right)^2\dfrac{1}{\left|\mathbf{r}-\mathbf{r}'\right|}, \text{if } \tau_{ij}<\left|\mathbf{r}-\mathbf{r}'\right|<R_i+R_j,\\ \dfrac{1}{\left|\mathbf{r}-\mathbf{r}'\right|}, \text{ if } R_i+R_j<\left|\mathbf{r}-\mathbf{r}'\right|\end{cases} \tag{24}$$

where $\tau_{ij}=\left|R_i-R_j\right|$ and $B_0=2\pi\left(4\pi R_iR_j\right)/\left(4\pi R_i^2\right)\left(4\pi R_j^2\right)$. The Coulomb potential decays slowly and long-range contributions to the free energy in a periodic system are not negligible. The Ewald summation technique is widely used to calculate the long-range contributions efficiently.[31] In this work, the Ewald summation technique is not applied to the Coulomb potential. Instead, since long-range contributions are very important in the formation of ordered nanostructure,[36] we introduce our approach to apply the Ewald summation technique in the context of the direct correlation function. The chemical potential from the Ewald summation is separately calculated and the direct correlation function is modified as

$$\begin{aligned}\mu_i^C(\mathbf{r})/k_BT &= -\sum_j \int d\mathbf{r}' C_{i,j}^C(\mathbf{r},\mathbf{r}')\rho_j(\mathbf{r}') \\ &= -\sum_j \int d\mathbf{r}' C_{i,j}^{C\prime}(\mathbf{r},\mathbf{r}')\rho_j(\mathbf{r}') + \mu_i^{C,ew}(\mathbf{r})\end{aligned} \tag{25}$$

and

$$C_{ij}^{C\prime}(\mathbf{r},\mathbf{r}') = C_{ij}^C(\mathbf{r},\mathbf{r}') + \frac{Z_i Z_j \Gamma}{|\mathbf{r}-\mathbf{r}'|} erf\left(\sqrt{\alpha}|\mathbf{r}-\mathbf{r}'|\right), \tag{26}$$

where the positive constant α in the error function $erf(x)$ determines the width of the Gaussian compensating charge distribution. The reciprocal space contribution, $\mu_i^{C,ew}(\mathbf{r})$ to the chemical potential from the Ewald summation is calculated by

$$\mu_i^{C,ew}(\mathbf{r})/k_BT = Z_i\Gamma\mathbf{FT}^{-1}\left[\frac{4\pi}{|\mathbf{k}|^2}\tilde{\rho}(\mathbf{k})\exp\left(-|\mathbf{k}|^2/4\alpha\right)\right], \tag{27}$$

where $\tilde{\rho}(\mathbf{k}) = \mathbf{FT}\left[\sum_j Z_j\rho_j(\mathbf{r})\right]$, $\mathbf{FT}$ and $\mathbf{FT}^{-1}$ are the Fourier and the inverse Fourier transformations. Since $1/|\mathbf{k}|^2$ is singular at $|\mathbf{k}| = 0$, $\tilde{\rho}(\mathbf{0})$ should be zero, *i.e.* the charge neutrality condition should be met. In an infinitely periodic system, the boundary condition at infinity affects the system free energy due to long-range Coulomb interactions and the resulting polarization energy should be considered.[31] Eq. (27) is valid for a system embedded in materials with infinite dielectric constant, *i.e.* metals. For a vacuum boundary condition, the polarization

energy needs to be included and the chemical potential field and the free energy become

$$\mu_i^{C,ew\prime}(\mathbf{r})/k_BT = \mu_i^{C,ew}(\mathbf{r})/k_BT + \frac{4\pi Z_i\Gamma}{3V}\left(\sum_j Z_j\int d\mathbf{r}'\mathbf{r}'\rho_j(\mathbf{r}')\right)\cdot\mathbf{r} \tag{28}$$

and

$$F^{ex\prime} = F^{ex} + \frac{2\pi\Gamma}{3V}\left|\sum_i Z_i\int d\mathbf{r}\mathbf{r}\rho_i(\mathbf{r})\right|^2. \tag{29}$$

2.5. Single molecular partition function

Here we discuss the single molecular partition function, Q, for the discrete limit and the linear configuration of monomer species as shown in Fig. 2. The extension to the continuous monomer segments as in SCFTs and configurations other than linear is discussed in Section 2.6. Q is given by

$$Q = \int d\mathbf{r}_1\cdots d\mathbf{r}_N K(\mathbf{r}_1,\cdots,\mathbf{r}_N)\exp\left\{-\sum_i^N w_i(\mathbf{r}_i)\right\}, \tag{30}$$

where K is the product of constraints between neighboring monomers

$$K(\mathbf{r}_1,\cdots,\mathbf{r}_N) = \prod_i^{N-1} P_i(\mathbf{r}_i,\mathbf{r}_{i+1}). \tag{31}$$

The bond length between neighboring monomers of polymers is usually approximated to follow a Gaussian distribution[45] and the constraint for the polymer configuration shown in Fig. 2A is given by

$$P_i(\mathbf{r},\mathbf{r}') = \left(\frac{3}{2\pi a_i^2}\right)^{3/2} \exp\left\{-\frac{3}{2a_i^2}(\mathbf{r}'-\mathbf{r})^2\right\}, \tag{32}$$

where a_i is the average distance between neighboring monomers, *i.e.* the Kuhn length. If the i th monomer is a HS as shown in Fig. 2B, the constraint is given by

$$P_i(\mathbf{r},\mathbf{r}') = \delta\left(|\mathbf{r}'-\mathbf{r}|-R\right)/4\pi R^2, \tag{33}$$

where R is the radius of the HS. To calculate Q, we introduce the segment distribution functions, $q_i(\mathbf{r})$ and $q_i^{\dagger}(\mathbf{r})$, defined as

$$q_{i+1}(\mathbf{r}) = \int d\mathbf{r}' G_i(\mathbf{r}',\mathbf{r}) q_i(\mathbf{r}') \tag{34}$$

and

$$q_i^{\dagger}(\mathbf{r}) = \int d\mathbf{r}' G_i(\mathbf{r},\mathbf{r}') q_{i+1}^{\dagger}(\mathbf{r}'), \tag{35}$$

where G_i is physically interpreted as the propagator from the i th monomer to the $i+1$ th one

toward the right in Fig. 2. The propagator, G_i is given by

$$G_i(\mathbf{r},\mathbf{r}') = \exp\left\{-w_i(\mathbf{r})/2\right\}P_i(\mathbf{r},\mathbf{r}')\exp\left\{-w_{i+1}(\mathbf{r}')/2\right\}. \tag{36}$$

Eqs. (34) and (35) can be numerically obtained from convolution of the distribution functions, q and $q^\dagger$, respectively, with the propagator, G, if boundary conditions are given such as,

$$q_1(\mathbf{r}) = \exp\left\{-w_1(\mathbf{r})/2\right\} \tag{37}$$

and

$$q_N^\dagger(\mathbf{r}) = \exp\left\{-w_N(\mathbf{r})/2\right\}. \tag{38}$$

Therefore, the distribution functions, q and $q^\dagger$, are obtained from the chemical potential fields, w, as shown in Fig. 1. Finally, Q is given as

$$Q = \int d\mathbf{r} q_i(\mathbf{r}) q_i^\dagger(\mathbf{r}), \tag{39}$$

where i can be arbitrarily chosen, since Eq. (39) is equal to Eq. (30) regardless of i. Physically, $q_i(\mathbf{r})$ and $q_i^\dagger(\mathbf{r})$ have the meaning of distribution functions of species i propagated from the free ends, $i = 1$ and $i = N$, respectively. The density function of monomer species i is obtained from Eq. (10) with the condition, $DF/Dw_i(\mathbf{r}) = 0$, as

$$\rho_i(\mathbf{r}) = \frac{n}{Q} q_i(\mathbf{r}) q_i^\dagger(\mathbf{r}). \tag{40}$$

Although we only introduced two kinds of constraint functions, one for polymers in Eq. (32), and the other for hard particles in Eq. (33), this formulation can be generalized to other constraints such as the continuous-segments propagator relevant for SCFTs (see Section 2.6) as well as to other monomer species such as non-isotropic Janus NPs. Furthermore, the approach can be applied to the mixed case of continuous and discrete segments as needed for ligand-stabilized NPs.[36] Such flexibility in the choice of monomer species and constraints clearly highlights the advantages and versatility of the proposed approach compared with previous SCFT, SCFT/DFT, and other polymer DFT approaches,[27,46] and allows us to simulate complex multi-component systems.

2.6. Numerical implementation

Eqs. (34) and (35) can be numerically evaluated using the convolution theorem as

$$\begin{aligned} q_{i+1}(\mathbf{r}) &= \exp\left\{-w_{i+1}(\mathbf{r})/2\right\} \\ &\times \mathbf{FT}^{-1}\left[\tilde{P}_i(\mathbf{k})\mathbf{FT}\left[\exp\left\{-w_i(\mathbf{r})/2\right\} q_i(\mathbf{r})\right]\right] \end{aligned} \tag{41}$$

and

$$\begin{aligned} q_i^\dagger(\mathbf{r}) &= \exp\left\{-w_i(\mathbf{r})/2\right\} \\ &\times \mathbf{FT}^{-1}\left[\tilde{P}_i(-\mathbf{k})\mathbf{FT}\left[\exp\left\{-w_{i+1}(\mathbf{r})/2\right\} q_{i+1}^\dagger(\mathbf{r})\right]\right], \end{aligned} \tag{42}$$

where $\tilde{P}_i(\mathbf{k}) = \mathbf{FT}\left[P_i(\mathbf{r})\right]$. However, in SCFTs, the propagator is modified for the continuous case and the parameter, i, becomes a continuous parameter. For clarity, we use s for the continuous parameter. The constraint function, $P_{i\leftrightarrow j}(\mathbf{r},\mathbf{r}')$, becomes

$$P_{i\leftrightarrow j}(\mathbf{r},\mathbf{r}') \propto \exp\left\{-\int_i^j ds \frac{3}{2a^2(s)}\left(\frac{d\mathbf{r}}{ds}\right)^2\right\} \tag{43}$$

and the propagator is given by the path integral

$$G_{i\leftrightarrow j}(\mathbf{r},\mathbf{r}') = \int \mathcal{D}\mathbf{r}'' \exp\left\{-\int_i^j ds\left[\frac{3}{2a^2(s)}\left(\frac{d\mathbf{r}''}{ds}\right)^2 + w_s(\mathbf{r}'')\right]\right\} \tag{44}$$

so that $q_s(\mathbf{r}) = \int d\mathbf{r}' G_{0\leftrightarrow s}(\mathbf{r}',\mathbf{r})$ and $q_s^\dagger(\mathbf{r}) = \int d\mathbf{r}' G_{s\leftrightarrow N}(\mathbf{r},\mathbf{r}')$. The molecular partition function Q can be obtained from $Q = \int d\mathbf{r} q_s(\mathbf{r}) q_s^\dagger(\mathbf{r})$, where s has any value between 0 and N. From the boundary conditions, $q_0(\mathbf{r}) = 1$ and $q_N^\dagger(\mathbf{r}) = 1$, one can obtain $q_s(\mathbf{r})$ and $q_s^\dagger(\mathbf{r})$ from the modified diffusion equations[20-21,45,47-49]

$$\frac{\partial q_s(\mathbf{r})}{\partial s} = \left\{\frac{a(s)^2}{6}\nabla^2 - w_s(\mathbf{r})\right\} q_s(\mathbf{r}) \tag{45}$$

and

$$-\frac{\partial q_s^{\dagger}(\mathbf{r})}{\partial s}=\left\{\frac{a(s)^2}{6}\nabla^2-w_s(\mathbf{r})\right\}q_s^{\dagger}(\mathbf{r}). \tag{46}$$

In this work, we utilize this functional form in order to account for the conformational entropy of polymers and ligands. Solving the diffusion equation is usually the most time consuming step in the iterations. The computation time required for the calculation is proportional to M^2, where M is the number of spatial grid points. Matsen *et al.* proposed a spectral method where $q_s(\mathbf{r})$ and $q_s^{\dagger}(\mathbf{r})$ are a linear combination of symmetry-adopted basis functions.[20] The method reduces the computational load dramatically but requires knowledge of the exact symmetry of the expected morphologies. Alternatively, the real space approach doesn't need such information and structures are obtained without any restriction of symmetry[19] but then the computational cost of calculating the partition function becomes extremely large. We adopt the real space approach but minimize the computational effort by implementing a recently developed algorithm, called the 'split step algorithm',[49] which extensively utilizes the Fast Fourier Transform (FFT). The basic scheme is given as

$$\begin{aligned} q_{s+ds}(\mathbf{r}) &= \exp\left\{-\frac{ds}{2}w_s(\mathbf{r})\right\}\exp\left[\frac{a^2}{6}ds\nabla^2\right] \\ &\times\exp\left\{-\frac{ds}{2}w_s(\mathbf{r})\right\}q_s(\mathbf{r}) \end{aligned} \tag{47}$$

and

$$q_{s-ds}^{\dagger}(\mathbf{r}) = \exp\left\{-\frac{ds}{2}w_s(\mathbf{r})\right\}\exp\left[\frac{a^2}{6}ds\nabla^2\right] \times \exp\left\{-\frac{ds}{2}w_s(\mathbf{r})\right\}q_s^{\dagger}(\mathbf{r}) \tag{48}$$

These equations can be numerically implemented as

$$q_{s+ds}(\mathbf{r}) = \exp\left\{-\frac{ds}{2}w_s(\mathbf{r})\right\} \times \mathbf{FT}^{-1}\left[\exp\left\{-\frac{a(s)^2}{6}ds|\mathbf{k}|^2\right\}\mathbf{FT}\left[\exp\left\{-\frac{ds}{2}w_s(\mathbf{r})\right\}q_s(\mathbf{r})\right]\right] \tag{49}$$

and

$$q_{s-ds}^{\dagger}(\mathbf{r}) = \exp\left\{-\frac{ds}{2}w_s(\mathbf{r})\right\} \times \mathbf{FT}^{-1}\left[\exp\left\{-\frac{a(s)^2}{6}ds|\mathbf{k}|^2\right\}\mathbf{FT}\left[\exp\left\{-\frac{ds}{2}w_s(\mathbf{r})\right\}q_s^{\dagger}(\mathbf{r})\right]\right] \tag{50}$$

(note that Eq. (49) is identical to Eq. (41), if the constraint function is given by Eq. (32)). Up to now, we have limited the discussion to the case of chains with a linear configuration. The extension to more complex configurations is identical to that reported for other polymer systems such as branched polymers[47-48] and is not repeated here. Since, in our work, monomer species can be soft molecules and hard molecules, multi-component molecular structures can be readily described by defining the monomer-monomer connectivity and specifying monomers with a parameter, i or s.

We adapted a numerical algorithm called the combinatorial screening technique by Drolet *et al.*[19] to iteratively solve Eqs. (8), (39), (34), (35), (40), and (14). The algorithm is illustrated in Fig. 1 and operates as follows. In the first step, we generate trial configurations of all species, $\rho(\mathbf{r})$, and obtain $w(\mathbf{r})$ from $\rho(\mathbf{r})$ using Eqs. (8) and (14). In the next step, new $\rho(\mathbf{r})$ are calculated from $w(\mathbf{r})$ of the previous step using Eqs. (39), (34), (35), and (40). Following this way, each step generates values for $w(\mathbf{r})$ and $\rho(\mathbf{r})$ from results of the previous step. This process is iterated until changes of $\rho(\mathbf{r})$ and $w(\mathbf{r})$ become sufficiently small. Since the free energy strongly depends on the box dimensions, we also minimize the system's free energy by varying the system size between iterations.[14] This procedure yields different solutions depending on the initial configurations. Thus, we perform these calculations with various initial configurations and choose the solution with the lowest free energy as the likely equilibrium phase.

2.7. Beyond the mean-field approximation

As shown in the previous sections, the numerical implementation is drastically simplified by the mean-field approximation, which is generally accurate for dense molecular systems. By limiting configurations to saddle points, the mean-field approximation greatly reduces the numerical complexity of the calculations. However, to properly describe dilute systems composed of small molecules, for example, a more advanced approach than the mean-field approach is required. In general, the chemical fields, w, and density functions, ρ, are complex (noting that w in Eq. (14) is a real function due to the mean-field approximation, see also relevant discussions in Refs. 50-51). Therefore, they cannot be calculated with the numerical

procedure given in Section 2.6. For such calculations, Ganesan *et al*. applied a complex Langevin dynamics for thermodynamic sampling.[50-51] We expect that such sampling method can be applied to our approach, since DFTs do not assume the mean-field approximation. Validation of these ideas is left for future work.

3. Simulation Results

3.1 HS Particle Behavior within BCPs

To test our theory for HS interactions, we compare our 1-dimensional predictions with the results obtained by Thompson *et al.*[28] using the DFT approach by Tarazona[52] for the same parameters. In this study, BCP composition is set to $f_A = 0.35$ and a typical value of 0.4655 is assigned for $N\rho_0^{-1}R_g^{-3}$, a parameter that specifies the volume of BCP relative to that of NPs. The radius of gyration of unperturbed BCPs, R_g, is the basic length unit in this work. The Flory-Huggins χN parameters are summarized in Table 1. We utilize the original form of the FMT approach and its hyper-netted chain (HNC) approximation form,[33,39,42] so that the $\mu_i^{HS}(\mathbf{r})/k_BT$ term in Eq. (14) becomes $-\sum_j \int d\mathbf{r}' C_{ij}^{HS}(\mathbf{r},\mathbf{r}')\rho_j(\mathbf{r}')$, where $C_{ij}^{HS}(\mathbf{r},\mathbf{r}')$ is the direct correlation function of the excess HS interaction free energy functional.[39] We examine two cases: large NPs, $R_p = 0.735\,R_g\,(=0.3\,R_0)$, with a small volume fraction, $\phi_p = 0.03$ (Fig. 3A), and small NPs, $R_p = 0.490\,R_g\,(=0.2\,R_0)$, with an intermediate volume fraction $\phi_p = 0.15$ (Fig. 3B), where R_0 is the unperturbed chain end-to-end distance of BCPs equal to $\sqrt{6}R_g$. For the case near the dilute limit, $\phi_p = 0.03$, all of the DFT approaches yield consistent results as shown in Fig. 3A. This is expected because both, the DFT by Tarazona[52] as well as the FMT approach, utilize virial

expansions of the excess chemical potential corresponding to pair exclusions at the dilute limit, and the HNC approximation is generally accurate if the density functional has small deviations from the reference state.[33,39,52] However, at the intermediate volume fraction of NPs, $\phi_p = 0.15$, shown in Fig. 3B, the results given by Thompson *et al.* [28] are in between those of the FMT and its HNC approximation form in terms of its shape and lamellar spacing. Compared with the FMT approach, the HS interactions of the DFT method by Tarazona[52] and HNC approximation are more repulsive. The discrepancy originates from the different functional forms of the excess free energy for HS interactions. A detailed discussion for those approaches can be found in Refs. 41-42.

3.2. Binary Mixture of Charged HS Particles near a Charged Hard Wall

To benchmark the accuracy of HS and Coulomb interactions in our approach, we calculate the double layer formation of HS particles with opposite charge to the surface charge of a hard wall and compare to results of previous simulations.[53-54] We study a binary mixture of charged HS particles near a charged hard wall. We add positively $(+)$ and negatively $(-)$ charged HS particles near a positively charged flat wall. The charges are fixed at $Z_+ = 1$ and $Z_- = -1$, and the Bjerrum length is set to $\Gamma = 19.8145\, d_0$ for the Coulomb potential, $\Phi(\mathbf{r}) / k_B T = \Gamma Z_i Z_j / |\mathbf{r}|$, where d_0 is the diameter of particles and the basic length unit in these simulations. The overall volume fractions of particles are set to $\phi_+ = 0.0462$ and $\phi_- = 0.0462$. The surface charge densities are given by $\sigma^* = 0.25$, 0.42, 0.55, and $0.7\, d_0^{-2}$. Figure 4 shows the formation of the double layer formation of negatively charged HS particles at high surface charge densities. This is consistent with previous exact Monte Carlo simulations for $\sigma^* = 0.7\, d_0^{-2}$,

shown as the open red circles in Fig. 4.[53] Results are further compared to a previous DFT study[55] that used the same surface charge densities, shown in the inset of Fig. 4. Our 1-dimensional simulation results correctly predict the position of the correlation peak but overestimate the particle density relative to the exact Monte Carlo simulation data. Deviations between these simulation and theoretical results are expected and are due to the different levels of approximations involved. The deviations between the predictions of the two theories arise from the different functional forms adopted for HS and long-range Coulomb interactions.

3.3. Self-assembly of two chemically distinct HS particles connected by a homopolymer molecule within BCPs

As an example of the Green function propagator for the mixed case of the continuous and discrete segments, we introduce two chemically distinct HS particles, p1 and p2, connected with a homopolymer, H, as well as A-B di-BCPs. We want to determine how the HS particle distribution in the A and B regions of the di-BCP depends on the length of the homopolymer H. For this molecule, the single molecular partition function is given by

$$Q \equiv \int d\mathbf{r}_{p1} \exp\left\{-w_{p1}\left(\mathbf{r}_{p1}\right)\right\} \iint d\mathbf{r}_0 d\mathbf{r}_{N_h} \frac{\delta\left(\left|\mathbf{r}_{p1}-\mathbf{r}_0\right|-R\right)}{4\pi R^2} G_H\left(\mathbf{r}_0, \mathbf{r}_{N_h}\right) \times \int d\mathbf{r}_{p2} \frac{\delta\left(\left|\mathbf{r}_{N_h}-\mathbf{r}_{p2}\right|-R\right)}{4\pi R^2} \exp\left\{-w_{p2}\left(\mathbf{r}_{p2}\right)\right\} \quad (51)$$

where G_H is the continuous propagator for the homopolymer H defined by Eq. (44). To obtain Q, we introduce the segment distribution functions, $q_i(\mathbf{r})$ and $q_i^{\dagger}(\mathbf{r})$ in Eqs. (34) and (35). The numerical calculation is performed using the equations,

$$q_{p1} = \exp\left\{-w_{p1}(\mathbf{r})\right\} \tag{52}$$

and

$$q_0(\mathbf{r}) = \mathbf{FT}^{-1}\left[\tilde{\delta}(\mathbf{k})\mathbf{FT}\left[q_{p1}(\mathbf{r})\right]\right], \tag{53}$$

where $\tilde{\delta}(\mathbf{k}) = \mathbf{FT}\left[\delta\left(|\mathbf{r}| - R\right)/4\pi R^2\right]$ and $q_0(\mathbf{r})$ is the segment distribution function of one end of the homopolymer propagated from the particle p1. The segment distribution functions of the homopolymer from $q_0(\mathbf{r})$ to $q_{N_h}(\mathbf{r})$ are calculated utilizing Eq. (45). The segment distribution $q_{p2}(\mathbf{r})$ is obtained from

$$q_{p2}(\mathbf{r}) = \exp\left\{-w_{p2}(\mathbf{r})\right\}\mathbf{FT}^{-1}\left[\tilde{\delta}(\mathbf{k})\mathbf{FT}\left[q_{N_h}(\mathbf{r})\right]\right]. \tag{54}$$

and the $q_i^{\dagger}(\mathbf{r})$ for the opposite direction from p2 to p1 are obtained using the same equations by replacing p1 with p2. To segregate p1 HS particle into block A and the p2 HS particle into block B, we set the χN parameters as shown in Table 2 (noting that for this simulation the χN parameters between the homopolymer and the two blocks were set equal to zero in order to clearly monitor the homopolymer size dependence). The radii of HS particles are fixed at $R_{p1} = R_{p2} = 0.735\, R_g$, *i.e.* identical to the simulation described in Fig. 3A for single NPs in only one block and the overall volume fraction of p1 and p2 particles in the system is set to $\phi_{p1} = \phi_{p2} = 0.03$. We assign a typical value of 0.4655 for $N\rho_0^{-1}R_g^{-3}$. For comparison, Fig. 4A shows the results of the simulations for HS particles without homopolymers. When a long

homopolymer with the size, $N_h / N = 0.5$, bridges two HS particles, the HS particles are slightly segregated to the edge of the blocks, *i.e.* towards the interface. In case of a short homopolymer bridge, $N_h / N = 0.1$, the segregation becomes significantly more pronounced. These results are physically reasonable, since shorter homopolymers are expected to bring two HS particles closer due to the smaller end-to-end chain length.

3.4. Ligand-stabilized NP / BCP self-assembly: bead-spring model of polymers and charged ligand effect on NP self-assembly behavior

In order to demonstrate flexibility of our methodology for incorporating complex molecular structures and interactions, we introduce NPs with charged ligands and BCPs represented by a bead-spring model where the BCP monomers have a hard-sphere core as shown in Fig. 6A. Firstly, we compare our bead-spring model with a comparable model system without hard-sphere cores, for which the system parameters are set to $f_A = 0.4$ and $\chi_{AB}N = 45$. For the hard spheres BCPs, A and B, we chose $N_A = 40$ and $N_B = 60$, equivalent to $f_A = 0.4$. The radius of a monomer is set to $R = 0.106R_g$, where $R_g = \sqrt{Na^2 / 6}$ and a is the Kuhn length set to $a = 0.245R_g$. The short-range interaction parameter is given by $\chi_{AB} / (4\pi R^3 / 3) = 80$ and the overall system volume fraction is given by 0.4. Fig. 6B shows the normalized volume fractions of monomers A and B. The overall shape of the lamellar self-assembly behavior is very similar. However, compared with SCFT, the bead-spring model of BCPs yields a larger lamellar spacing. This is due to the more extended conformations of the polymers represented by the bead-spring model arising from excluded volume interactions between monomer units, compared to those for

unperturbed polymer models, as expected theoretically.[45] Having established our bead-spring model, we add NPs with charged ligands and counter anions (CAs) satisfying the charge neutrality condition. The overall volume fraction of ligand-stabilized NPs and CAs is set to 0.08, while the value of BCPs is set to 0.32. The radius of NPs is given by $R_{NP} = 0.530$ and the number of ligands per NP is set to $n_{Ligand} = 20$. The ligands are composed of 5 HSs with the radius equal to that of the BCP monomers and the terminal HSs have a positive charge $Z_+ = 1$ as shown in Fig. 7A. CAs have a negative charge $Z_- = -1$. As discussed in Section 2.4, the boundary condition at infinity affects the overall system energy in case of the long-range Coulomb potential. In our simulation, the vacuum boundary condition was assumed. The interaction parameters are summarized in Table 3. The single molecular partition function of the ligand-stabilized NPs shown in Fig. 7A is given by

$$Q \equiv \int d\mathbf{r}_{NP} \exp\left\{-w_{NP}\left(\mathbf{r}_{NP}\right)\right\}\left[\int d\mathbf{r}_i d\mathbf{r}_{N_{Ligand}} \frac{\delta\left(\left|\mathbf{r}_{NP}-\mathbf{r}_i\right|-R_{NP}-R\right)}{4\pi\left(R_{NP}+R\right)} G_{Ligand}\left(\mathbf{r}_i, \mathbf{r}_{N_{Ligand}}\right)\right]^{n_{Ligand}}, \quad (55)$$

where $G_{Ligand}\left(\mathbf{r}_i, \mathbf{r}_{N_{Ligand}}\right)$ is the propagator from one ligand chain end i to the other end N_{Ligand}. The first step is to obtain $q_i^{\dagger}\left(\mathbf{r}\right)$ for the ligand monomer i in Fig. 7A from the boundary condition, $q_{N_{Ligand}}^{\dagger}\left(\mathbf{r}\right) = \exp\left\{-w_{N_{Ligand}}\left(\mathbf{r}\right)/2\right\}$ using Eq. (36) with the Gaussian constraint given in Eq. (32). Then $q_{NP}^{\dagger}\left(\mathbf{r}\right)$, $q_{NP}\left(\mathbf{r}\right)$, and $q_i\left(\mathbf{r}\right)$ are calculated using the following equations,

$$q_{NP}^{\dagger}\left(\mathbf{r}\right) = \exp\left\{-w_{NP}\left(\mathbf{r}\right)/2\right\}\left\{\mathbf{FT}^{-1}\left[\tilde{\delta}\left(\mathbf{k}\right)\mathbf{FT}\left[q_i^{\dagger}\left(\mathbf{r}\right)\right]\right]\right\}, \quad (56)$$

$$q_{NP}(\mathbf{r}) = \exp\left\{-w_{NP}(\mathbf{r})/2\right\}\mathbf{FT}^{-1}\left[\tilde{\delta}(\mathbf{k})\mathbf{FT}\left[q_i^{\dagger}(\mathbf{r})\right]\right]^{n_{Ligand}-1}, \quad (57)$$

and

$$q_i(\mathbf{r}) = \exp\left\{-w_i(\mathbf{r})/2\right\}\mathbf{FT}^{-1}\left[\tilde{\delta}(\mathbf{k})\mathbf{FT}\left[q_{NP}(\mathbf{r})\right]\right], \quad (58)$$

where $\tilde{\delta}(\mathbf{k}) = \mathbf{FT}\left[\delta\left(|\mathbf{r}| - R_{NP} - R\right)/4\pi\left(R_{NP}+R\right)^2\right]$. Finally, other ligand components, $q_{i+1}\cdots q_{N_{Ligand}}$, can be calculated using Eq. (36) with the Gaussian constraint. Two different conditions are studied: (i) no Coulomb interactions, *i.e.* $\Gamma = 0$ and (ii) Coulomb interaction with $\Gamma = 7.0R_g$, which corresponds to a typical dielectric constant of a polymeric materials with $R_g = 5\,nm$ at room temperature of $\varepsilon_r = 20$. In the absence of Coulomb interactions ($\Gamma = 0$), NPs are highly localized within block A as shown in Fig. 7B due to a very weak entropic driving force of mixing (noting that the volume ratio of NPs to BCPs is 2.25). When the Coulomb potential is applied by setting $\Gamma = 7.0R_g$, the NP-NP repulsion forces become stronger and NPs are more dispersed (compare Fig. 7D and 7E). Such repulsive interactions between ligands can lead to an enhanced dispersion of NPs when they are mixed with BCPs.[13,58] The density profile of CAs are shown in Fig. 7F and Fig. 7G. Due to the long-range Coulomb interactions, CAs and NPs form an ordered structure where CAs localize between NPs to screen the Coulombic repulsive force among NPs. Such ordered NP localization in BCPs has not been experimentally observed to date and is intriguing. Future work will include a full study of this phenomenon.

4. Conclusion

We presented a theoretical framework that unifies polymer self-consistent field theory and density functional theory that incorporates the complexity of hybrid molecular structures and their interactions. The Green function propagator was extended to hard particles for describing multi-component molecules composed of soft and hard chemical species. Furthermore, direct correlation functions used in DFTs were utilized to describe key physical interactions including long-range Coulomb and HS interactions. To validate our approach, we compared our results with two previous simulation studies: (i) the NP segregation behavior within BCPs and (ii) the double layer formation of charged HS particles near a charged wall. In both cases, we obtained good agreement with previously reported results on these systems. We then applied our approach to demonstrate the self-assembly of two chemically distinct NPs connected by a polymer molecule within the phase-separated BCPs. Finally, we investigated a model system for the self-assembly of BCPs and NPs with charged ligands. Due to sampling efficiency of phase space and descriptive power of molecular structures and interactions, we expect that our approach will vastly improve our ability to simulate large complex systems without loss of molecular details. Our approach is based on the mean-field approximation. To overcome the limitations of the mean-field approximation such as the neglect of thermal fluctuations, we expect that our method can be combined with a recent field theoretic approach[50] that goes beyond the mean-field approximation. Future research will include systems with dipole interactions between NPs and various polymeric systems with unique architectures.

Acknowledgements

This publication was based on work supported by Award No. KUS-C1-018-02, made by King Abdullah University of Science and Technology (KAUST). The calculations have been performed using computational resources of the Computational Center for Nanotechnology Innovation (CCNI) at Rensselaer Polytechnic Institute.

References

[1] D. J. Norris, A. L. Efros, and S. C. Erwin, Science **319** (5871), 1776 (2008).
[2] T. Hyeon, S. S. Lee, J. Park, Y. Chung, and H. B. Na, J. Am. Chem. Soc. **123** (51), 12798 (2001).
[3] V. F. Puntes, K. M. Krishnan, and A. P. Alivisatos, Science **291** (5511), 2115 (2001).
[4] H. Zheng, R. K. Smith, Y.-w. Jun, C. Kisielowski, U. Dahmen, and A. P. Alivisatos, Science **324** (5932), 1309 (2009).
[5] M. L. Steigerwald, A. P. Alivisatos, J. M. Gibson, T. D. Harris, R. Kortan, A. J. Muller, A. M. Thayer, T. M. Duncan, D. C. Douglass, and L. E. Brus, J. Am. Chem. Soc. **110** (10), 3046 (1988).
[6] I. Gur, N. A. Fromer, M. L. Geier, and A. P. Alivisatos, Science **310** (5747), 462 (2005).
[7] F. X. Redl, K. S. Cho, C. B. Murray, and S. O'Brien, Nature **423** (6943), 968 (2003).
[8] E. V. Shevchenko, D. V. Talapin, N. A. Kotov, S. O'Brien, and C. B. Murray, Nature **439** (7072), 55 (2006).
[9] M. A. Noginov, G. Zhu, A. M. Belgrave, R. Bakker, V. M. Shalaev, E. E. Narimanov, S. Stout, E. Herz, T. Suteewong, and U. Wiesner, Nature **460** (7259), 1110 (2009).
[10] D. Gebauer, A. Volkel, and H. Colfen, Science **322** (5909), 1819 (2008).
[11] E. M. Pouget, P. H. H. Bomans, J. A. C. M. Goos, P. M. Frederik, G. de With, and N. A. J. M. Sommerdijk, Science **323** (5920), 1455 (2009).
[12] S. C. Warren, F. J. DiSalvo, and U. Wiesner, Nature Mater. **6** (2), 156 (2007).
[13] S. C. Warren, L. C. Messina, L. S. Slaughter, M. Kamperman, Q. Zhou, S. M. Gruner, F. J. DiSalvo, and U. Wiesner, Science **320** (5884), 1748 (2008).
[14] Y. Bohbot-Raviv and Z.-G. Wang, Phys. Rev. Lett. **85** (16), 3428 (2000).
[15] F. J. Martínez-Veracoechea and F. A. Escobedo, Macromolecules **42** (5), 1775 (2009).
[16] F. J. Martínez-Veracoechea and F. A. Escobedo, Macromolecules **40** (20), 7354 (2007).
[17] F. J. Martínez-Veracoechea and F. A. Escobedo, J. Chem. Phys. **125** (10), 104907 (2006).
[18] T. Dotera, Phys. Rev. Lett. **89** (20), 205502 (2002).
[19] F. i. Drolet and G. H. Fredrickson, Phys. Rev. Lett. **83** (21), 4317 (1999).
[20] M. W. Matsen and M. Schick, Phys. Rev. Lett. **72** (16), 2660 (1994).
[21] E. Helfand, J. Chem. Phys. **62** (3), 999 (1975).
[22] C. A. Tyler, J. Qin, F. S. Bates, and D. C. Morse, Macromolecules **40** (13), 4654 (2007).
[23] Z. Guo, G. Zhang, F. Qiu, H. Zhang, Y. Yang, and A.-C. Shi, Phys. Rev. Lett. **101** (2), 028301 (2008).
[24] S. W. Sides, B. J. Kim, E. J. Kramer, and G. H. Fredrickson, Phys. Rev. Lett. **96** (25),

250601 (2006).
[25] A. Bymaster, S. Jain, and W. G. Chapman, J. Chem. Phys. **128** (16), 164910 (2008).
[26] S. Jain, P. Jog, J. Weinhold, R. Srivastava, and W. G. Chapman, J. Chem. Phys. **128** (15), 154910 (2008).
[27] S. Tripathi and W. G. Chapman, Phys. Rev. Lett. **94** (8), 087801 (2005).
[28] R. B. Thompson, V. V. Ginzburg, M. W. Matsen, and A. C. Balazs, Science **292** (5526), 2469 (2001).
[29] R. B. Thompson, V. V. Ginzburg, M. W. Matsen, and A. C. Balazs, Macromolecules **35** (3), 1060 (2002).
[30] L. Zhang, J. Lin, and S. Lin, Macromolecules **40** (15), 5582 (2007).
[31] D. Frenkel and B. Smit, *Understanding molecular simulation : from algorithms to applications*, 2nd ed. (Academic Press, San Diego, 2002).
[32] K. Hiroike, Mol. Phys. **33** (4), 1195 (1977).
[33] Y. Rosenfeld, J. Chem. Phys. **98** (10), 8126 (1993).
[34] Y. Rosenfeld and L. Blum, J. Chem. Phys. **85** (3), 1556 (1986).
[35] S. M. Foiles and N. W. Ashcroft, J. Chem. Phys. **75** (7), 3594 (1981).
[36] K. Hur, R. G. Hennig, F. Escobedo, and U. Wiesner, (unpublished).
[37] K. M. Hong and J. Noolandi, Macromolecules **14** (3), 727 (1981).
[38] G. H. Fredrickson, Soft Matter **3** (11), 1329 (2007).
[39] Y. Rosenfeld, Phys. Rev. Lett. **63** (9), 980 (1989).
[40] J. K. Percus, J. of Stat. Phys. **15** (6), 505 (1976).
[41] P. Tarazona, J. A. Cuesta, and Y. Martinez-Raton, Lect. Notes Phys. **753**, 247 (2008).
[42] J. P. Hansen and I. R. McDonald, *Theory of simple liquids*, 2nd. ed. (Academic Press, London ; Orlando, 1986).
[43] L. Blum, Mol. Phys. **30** (5), 1529 (1975).
[44] L. Blum and Y. Rosenfeld, J. of Stat. Phys. **63** (5-6), 1177 (1991).
[45] M. Doi and S. F. Edwards, *The theory of polymer dynamics*. (Clarendon Press ; Oxford University Press, Oxford [Oxfordshire] New York, 1986).
[46] Y.-X. Yu and J. Wu, J. Chem. Phys. **117** (5), 2368 (2002).
[47] G. M. Grason, B. A. DiDonna, and R. D. Kamien, Phys. Rev. Lett. **91** (5), 058304 (2003).
[48] G. M. Grason and R. D. Kamien, Phys. Rev. E **71** (5), 051801 (2005).
[49] G. Tzeremes, K. Rasmussen, T. Lookman, and A. Saxena, Phys. Rev. E **65** (4), 041806 (2002).
[50] G. H. Fredrickson, V. Ganesan, and F. Drolet, Macromolecules **35** (1), 16 (2001).
[51] V. Ganesan and G. H. Fredrickson, Europhys. Lett. **55** (6), 814 (2001).
[52] P. Tarazona, Mol. Phys. **52** (1), 81 (1984).
[53] P. Ballone, G. Pastore, and M. P. Tosi, J. Chem. Phys. **85** (5), 2943 (1986).
[54] G. M. Torrie and J. P. Valleau, Chem. Phys. Lett. **65** (2), 343 (1979).
[55] R. D. Groot, Phys. Rev. A **37** (9), 3456 (1988).
[56] A.-C. Shi and J. Noolandi, Macromol. Theory and Simul. **8** (3), 214 (1999).
[57] Q. Wang, T. Taniguchi, and G. H. Fredrickson, J. Phys. Chem. B **108** (21), 6733 (2004).
[58] S. Warren, M. Banholzer, L. Slaughter, E. Giannelis, F. DiSalvo, and U. Wiesner. J. Am. Chem. Soc., **128** (37), 12074 (2006).

Tables

TABLE 1. Flory-Huggins χN parameters for the simulation of HS particle self-assembly within BCPs.

χN	B	P
A	20	0
B		20

TABLE 2. Flory-Huggins χN parameters for the simulation of self-assembly of two chemically distinct HS particles connected by a homopolymer molecule within BCPs

χN	B	p1	p2	H
A	20	0	20	0
B		20	0	0
p1			20	0
p2				0

TABLE 3. Flory-Huggins χ parameters for the self-assembly of BCPs and NPs with charged ligands

$\chi / (4\pi R^3 / 3)$	B	NP	Ligand	CA

A	80	0	0	0
B		80	80	80
NP			0	0
Ligands				0

Figure Legends

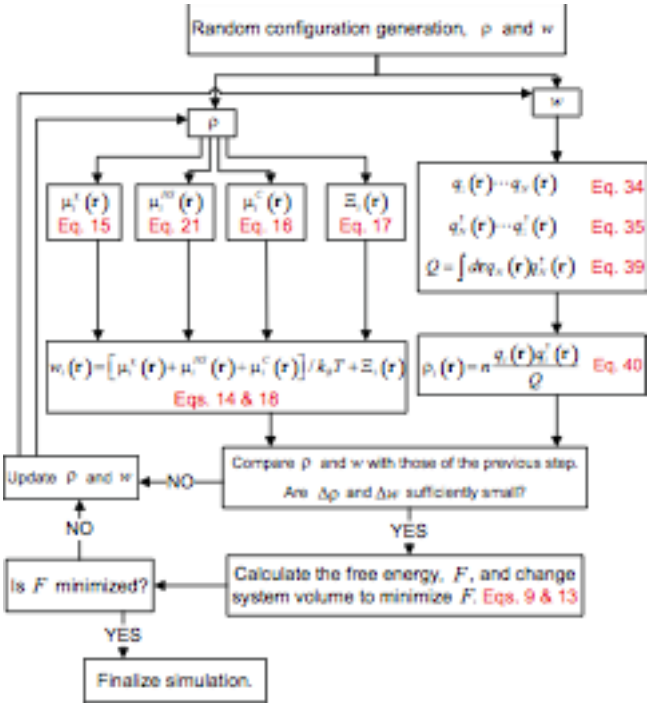

FIG. 1. The general schematic procedure and key equations of the present approach for a homogeneous system of n molecules composed of N monomers specified as i.

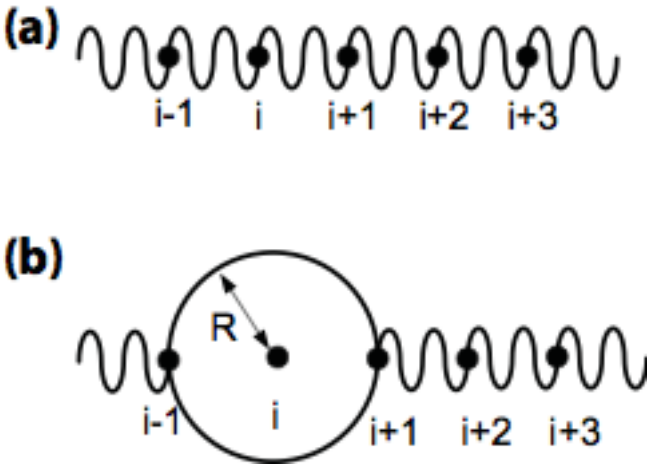

FIG. 2. Multi-component molecule representations with the linear configuration for **(a)** flexible monomers and **(b)** HS particles with flexible molecules

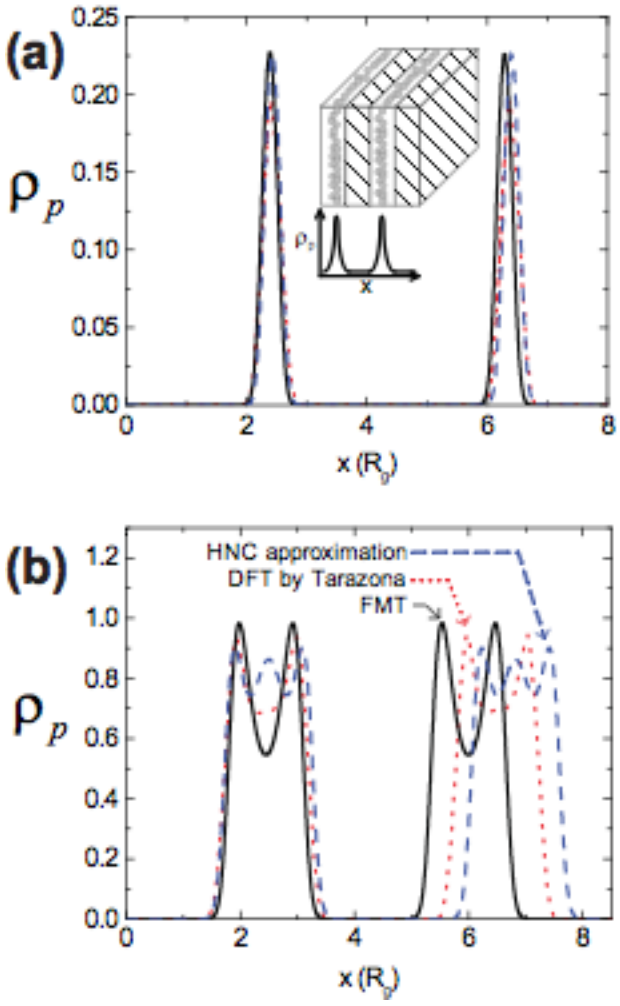

FIG. 3. Comparison of particle density profiles, ρ_p, in the lamellar morphology of BCP/NP self-assembly varying the excess HS free energy functional. We verify our approach by comparing with results of previous calculations.[28] Black solid lines are results applying the FMT, blue dashed lines results from the HNC approximation form of the FMT, and red dotted lines results from applying the DFT by Tarazona, see Ref. 28. **(a)** Large particles at the dilute condition ($R_p = 0.735\, R_g$, $\phi_p = 0.03$). **(b)** Small particles with intermediate volume fraction ($R_p = 0.490\, R_g$, $\phi_p = 0.15$). Compared with the FMT approach, the HS interactions of the DFT approach by Tarazona[52] and HNC approximation are more repulsive. The discrepancy originates from different functional forms of the excess free energy for HS interactions.

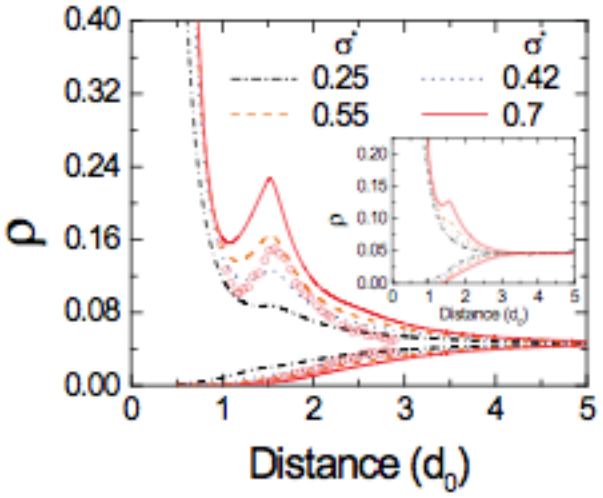

FIG. 4. Density profiles of positively charged, ρ_+, and negatively charged HS particles, ρ_-, as a function of distance from a positively charged flat wall with different surface charge densities, $\sigma^* = 0.25$, 0.42, 0.55, and $0.7\ d_0^{-2}$ (bottom to top for ρ_- and top to bottom for ρ_+), where d_0 is the diameter of HS particles. Open red circles are Monte Carlo simulation results of Ballone *et al*. at $\sigma^* = 0.7\ d_0^{-2}$.[53] The inset displays results from R. Groot.[55] The double layer formation is observed at high surface charge densities.

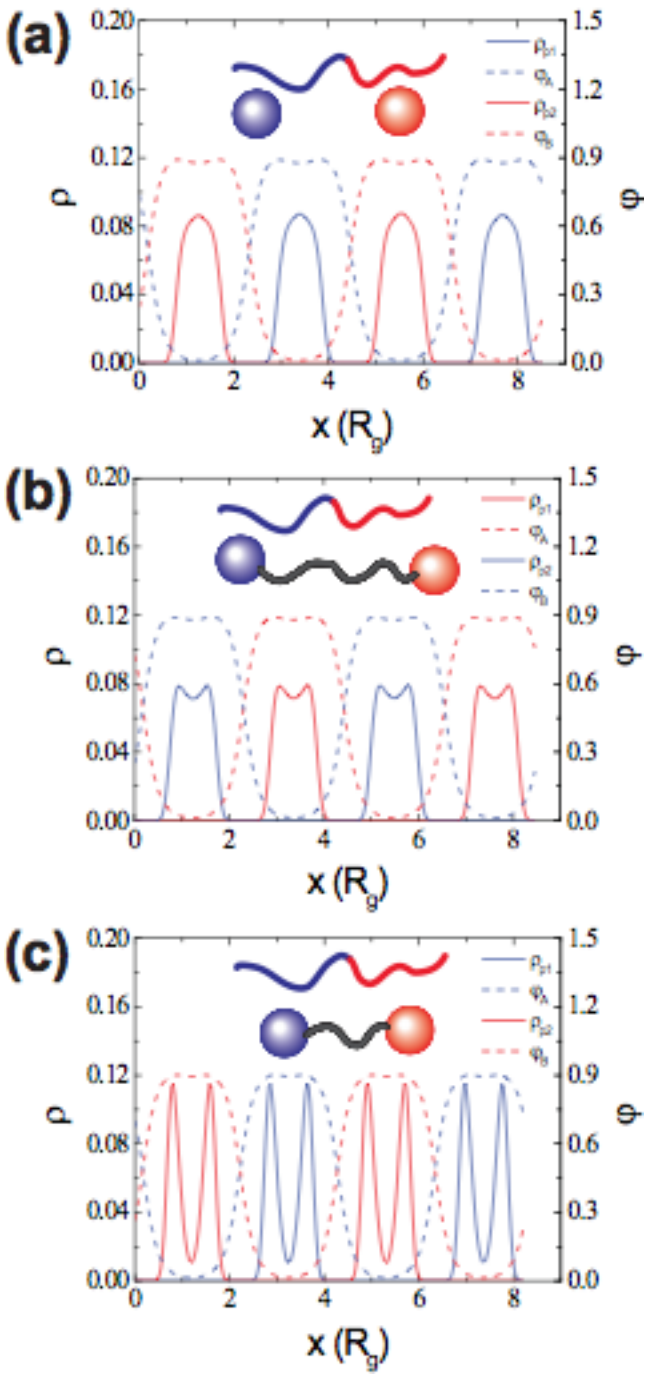

FIG. 5. Density profiles of NPs, ρ, and local volume fractions of BCPs, φ. The solid blue lines depict ρ of the p1-type NPs and the solid red lines show ρ of the p2-type NPs. The dotted blue lines represent φ of block A and the red lines show φ of block B. **(a)** Free NPs. **(b,c)** NPs connected by a homopolymer molecule with size **(b)** $N_h / N = 0.5$ and **(c)** $N_h / N = 0.1$.

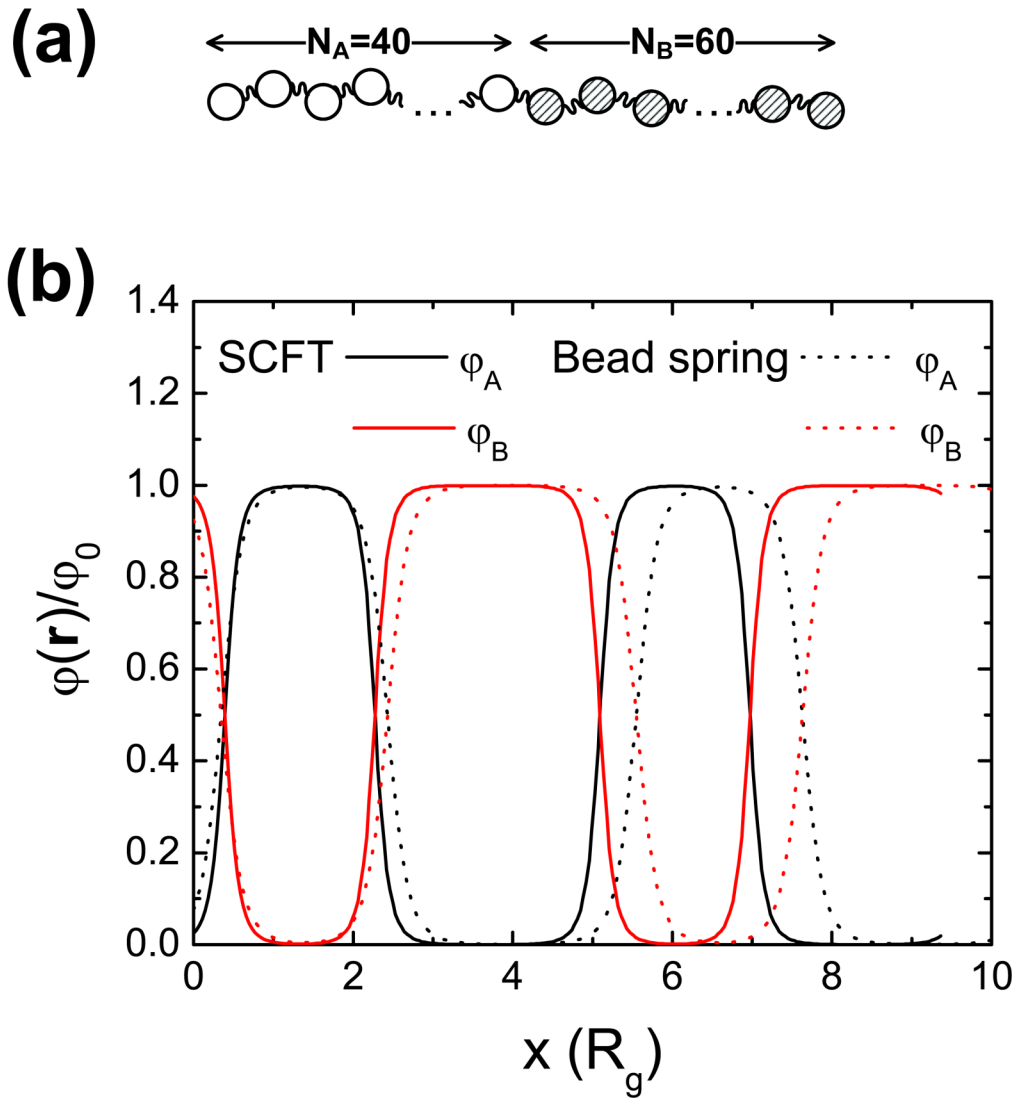

FIG. 6. Comparison of the bead-spring model and SCFT. The bead-spring model exhibits a larger lamellar spacing due to excluded volume interactions between monomer units. **(a)** Illustration of the bead-spring representation of a BCP. **(b)** Normalized local volume fractions of block A (black) and block B (red). The solid lines are results of SCFT and the dotted lines are those of the bead-spring model.

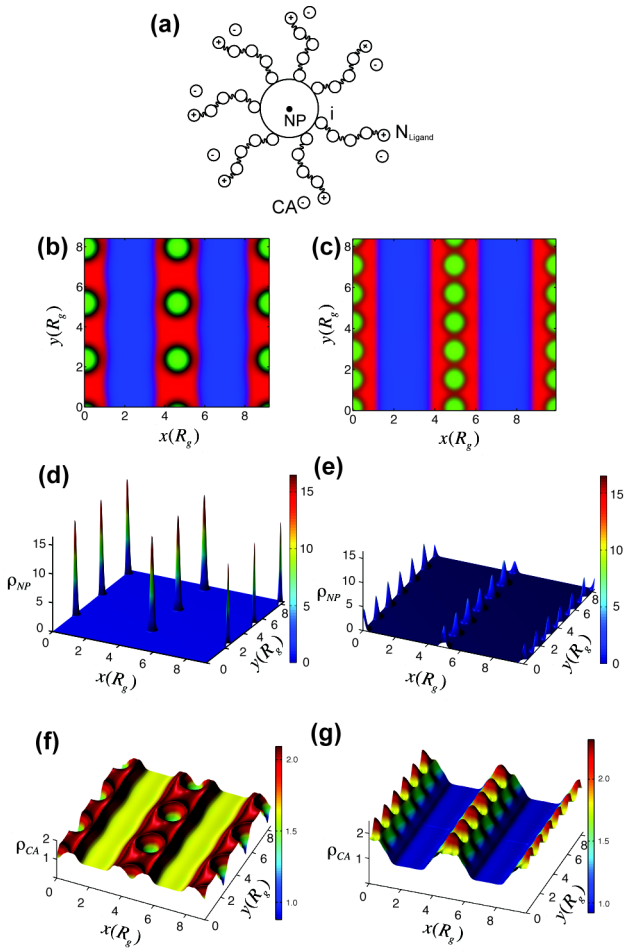

FIG. 7. Self-assembly of BCPs, NPs with charged ligands, and CAs, illustrating the effect of NP Coulomb repulsions on enhancing the regular dispersion of NPs. **(a)** Illustration of NPs with charged ligands and CAs. **(b,c)** Red color represents block A, blue color block B, and green color NPs with ligands. Density profiles of **(d,e)** NPs and **(f,g)** CAs. Two different conditions are studied by varying the parameter Γ: **(b,d,f)** $\Gamma = 0$, **(c,e,g)** $\Gamma = 7.0R_g$.